Flow-induced deformation of shallow microfluidic channels

Thomas Gervais,[a] Jamil El-Ali,[b] Axel Günther[b] and Klavs F. Jensen*[b]

We study the elastic deformation of poly(dimethylsiloxane) (PDMS) microchannels under imposed flow rates and the effect of this deformation on the laminar flow profile and pressure distribution within the channels. Deformation is demonstrated to be an important consideration in low aspect ratio (height to width) channels and the effect becomes increasingly pronounced for very shallow channels. Bulging channels are imaged under varying flow conditions by confocal microscopy. The deformation is related to the pressure and is thus non-uniform throughout the channel, with tapering occuring along the stream-wise axis. The measured pressure drop is monitored as a function of the imposed flow rate. For a given pressure drop, the corresponding flow rate in a deforming channel is found to be several times higher than expected in a non-deforming channel. The experimental results are supported by scaling analysis and computational fluid dynamics simulations coupled to materials deformation models.

Introduction

Soft lithography techniques offer a valuable alternative to conventional lithography for a wide range of microfluidic applications.[1] Poly(dimethylsiloxane) (PDMS) is often the material of choice as it is quick and simple to use, cheap, transparent, and biocompatible.[2] PDMS can be molded to yield features down to the nanometre scale, allowing the creation of nanochannels and structures,[3] microcontact printing stamps,[4] and other devices requiring fine geometric control.

An inherent property of soft lithography, which sets it apart from classical silicon- or glass-based micromachining processes, is the high compliance of PDMS. The bulk properties of PDMS are characterized by a low Young's modulus E (in the range of 0.5 to 4 MPa depending upon curing conditions) and a high Poisson ratio ($v = 0.5$, *i.e.* essentially incompressible), making it a typical rubber elastic material.[5] One-dimensional stress–strain analysis implies a structural deformation (strain) on the order of 10% under a pressure of 1 atm. In contrast, Young's modulus for single crystalline silicon ($E = 170$ GPa) is several orders of magnitude above that of PDMS, and the material can withhold extremely high pressures without deforming.[6]

The rubber elastic properties of PDMS have provided new opportunities for microfluidic devices. Quake and co-workers have demonstrated how PDMS can be used to design pressure-actuated valves and create a versatile fluidic control platform.[7,8] Similarly, deformable "soft" microdevices have been used in micro flow cytometry,[9] on-chip peristaltic pumping and mixing[10] and pressure sensors.[11]

On the other hand, the deformation of rubber elastic materials also limits the range of applications of soft lithography. The sagging and sticking of structures with very low aspect ratios (height/width) will impose constraints on how wide channels can be made[12] and structural analysis has been performed to further understand this phenomenon in the specific case of microcontact printing.[13]

Similarly, for pressure-driven flows, low aspect ratio channels will have a tendency to bulge under the imposed pressure. The deformation of a microfluidic channel drastically affects the effective pressure drop across it and the resulting flow profile, since the hydraulic resistance has a fourth power dependence on the cross-section length scale.[14] Consequently, any microfluidic applications for which a precise knowledge of the flow profile, pressure, and channel geometry is critical will be compromised if the actual channel deformation has not been quantified.

The effect of channel deformation becomes important in a number of common microfluidic applications. Cellular[15,16] and protein[17] shear-flow assays with linear velocities of the order of 1 m s^{-1} are examples for which the actual flow profile needs to be determined accurately in order to compute the effective shear rate. Diffusion-limited mass transfer also depends on flow profile and channel height.[18] For a pressure-driven flow with specified pressure drop, the Péclet number $Pe = UL/D$ (ratio of convective to diffusive time scales) varies as h^2 in a Poiseuille flow profile (see Table 1). The increase in the channel's effective height thus increases Taylor dispersion and affects the ability of a system to resolve intrinsic surface kinetics such as in surface plasmon resonance (SPR) sensing

Table 1 Cross-section dependence of key quantities susceptible to channel deformation in low aspect ratio microfluidic devices ($W \gg h$) for both fixed pressure drop and fixed flow rate conditions

Effect	Variable	Fixed Δp	Fixed Q
Fluid velocity	U	$\sim h^2$	$\sim h^{-1} W^{-1}$
Shear stress	τ	$\sim h$	$\sim h^{-2} W^{-1}$
Residence time	t	$\sim h^{-2}$	$\sim h\, W$
Dispersion	Pe	$\sim h^2$	$\sim h^{-1} W^{-1}$

[a] Dept. of Biological Engineering, MIT, 77 Massachusetts Avenue, Cambridge, MA 02139, USA. E-mail: tgervais@mit.edu
[b] Dept. of Chemical Engineering, MIT, 77 Massachusetts Avenue, Cambridge, MA 02139, USA. E-mail: kfjensen@mit.edu; Fax: +1-617-258-8224; Tel: +1-617-253-4589

technology.[19] In nanolitre-size SPR sensors,[20] the increase in the hydraulic resistance of the device yields higher pressures for the same flow rate and induces potential channel deformation. Multiphase microfluidic systems for the study of fast chemical reaction kinetics or crystallization often rely on droplet-based flows through microchannels at high velocities (>0.1 m s^{-1}).[21] Deformation also affects absorption measurements, which depend exponentially on the optical path length across the channel. Thus, many characteristics of microfluidics (e.g., fluid velocity, shear stress, residence time, and dispersion) are sensitive to channel dimensions[22] (Table 1) and will be influenced by channel deformation.

Few studies have discussed the importance of bulk channel deformation in microfluidics. Holden et al. used the change in fluorescence intensity with channel bulging to quantify experimentally bulk PDMS deformation under high pressure drop (~1 atm).[23] Hosokawa et al. have monitored pressure changes in microchannels using deformable PDMS gratings.[11] However, neither of these analyses provides a structural model to describe the magnitude of the channel bulging with respect to the imposed flow rate (or pressure) and channel geometry.

Herein we provide theoretical and experimental verification of the extent of PDMS deformation inside rectangular microchannels. Finite element analysis is used to model the expected deformation and to extract scaling relationships between the expected deformation and the operating conditions. These scaling laws should be useful to experimentalists as design constraints to either avoid deformation or to exploit deformation in future devices.

Theory

The primary aspect of the model described in this section is the coupling of the laminar flow to the structural deformation through the hydrodynamic pressure exerted at the liquid–solid interface (Fig. 1). The model is first presented in decoupled form and a description of the coupling is provided afterwards.
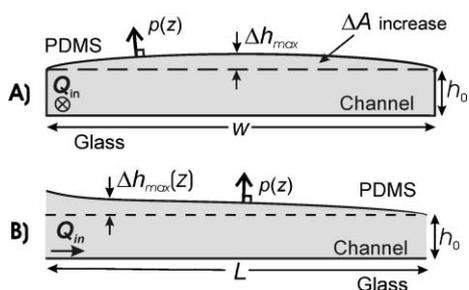

Fig. 1 Schematic representation of polymer channel deformation under an imposed flow rate. A) Channel cross-section normal to flow: Imposed pressure makes the cross-sectional area increase, thus deforming the flow profile inside the device and lowering the channel's hydraulic resistance. B) Channel cross-section parallel to flow. The bulging of the channel becomes attenuated as the outlet is approached since the pressure decreases to ambient value. For a fixed flow rate, an acceleration of the fluid is expected along the length as a result of the decreasing cross-sectional area.

Steady laminar flow

Flow in a microfluidic channel is described by the steady-state Navier–Stokes equation:

$$-\rho \, \vec{v}\vec{\nabla}\cdot\vec{v} + \mu\vec{\nabla}^2 \, \vec{v} = \vec{\nabla}p \tag{1}$$

Here ρ is the fluid density, $\vec{v}$ is the fluid velocity, p is the applied pressure and μ is the fluid viscosity (assumed to be that of water in this study: $\mu = 0.001$ Pa s). For low aspect ratio rectangular channels with an imposed volumetric flow rate Q of an incompressible liquid, solving eqn (1) and averaging over the cross-section yields a relationship between the flow rate and the pressure of the form:[14]

$$-\frac{\partial p(z)}{\partial z} = \frac{12\mu}{h^3 W} Q \tag{2}$$

where $p(z)$ is the pressure at stream-wise position z and A is the cross-sectional area. The dependence of the pressure drop on the channel height to the third power gives a strong sensitivity to channel deformation.

Structural mechanics

At any cross-section along the channel (z-direction), the pressure $p(z)$ will cause the channel to expand if we assume the surface to elastically deform according to its Young's modulus E. In this particular case, the glass slide is assumed rigid ($E_{SiO_2} = 62$ GPa) and the channel perfectly sealed, thereby imposing a zero-displacement boundary condition along the rubber/glass interface. Inside the channel, the boundary condition is replaced by a fixed pressure on the deformable channel walls. In most applications, the thickness of the PDMS slab (several millimetres) is much larger than the channel dimensions, so that the structural displacement of the PDMS can be assumed to take place in a semi-infinite medium. The problem can then be modeled using the constitutive stress–strain and strain–displacement coupled equations with proper boundary conditions accounting for fixed displacement at the edges and fixed pressure at the flow interface. Stress–strain analysis in semi-infinite media is common in soil mechanics, where the pressure imposed by a large structure causes the soil to deform around it (see for example Poulos[24]).

The mathematical formulation of this classical structural mechanics problem involves 15 coupled differential equations (6 stresses, 6 strains, 3 displacements) for which analytic solutions exist only in the cases of high symmetry (see Appendix for the vectorial form of the stress–displacement equations and their boundary conditions). For example, analytic solutions exist if the displacement conditions are relaxed, i.e., the PDMS is not bound to the glass. This situation would lead to a variant of the Boussinesq contact problem: a semi-infinite elastic medium moving under a point force.[25] However, the presence of a mixed boundary condition (pressure and displacement) in the present case is an indicator that analytic methods will be difficult to apply.[26] Therefore, numerical simulations are used to obtain a useful solution to these equations.

Fluid flow–structure interactions

The strong coupling between the flow solution and the structural deformation derives from the third power dependence of the channel height on the pressure drop in an approximately rectangular channel with $W \gg h$. Under an imposed flow rate, the pressure distribution inside the channel will cause the structure to deform. The deformation induced in the channel cross-section will, in turn, modify the fluid velocity and the pressure distribution, which drives fluid channel deformation and so on. Since the hydrostatic pressure is higher near the inlet than at the outlet, the channel deformation is expected to vary along the channel's main axis.

Small displacement approximation and scaling analysis

Since the system of equations is too complex to be solved analytically, a scaling approximation based on physical reasoning is needed to estimate the amount of deformation sustained in the channels. To obtain such a solution, we start by assuming that the maximum strain in the system will be on the order of the one provided by Hooke's law: $\varepsilon = \sigma / E$. In an infinite medium, all strains are expected to vanish very far from the deforming region. In this particular problem, the characteristic length scale of strain decay is proportional to the width W of the channel, and not to the height.[27] Since the maximum stress observed in the system is proportional to the pressure, the stress–strain scale in the problem becomes

$$\varepsilon_{vertical} \sim \frac{\Delta h}{W} \sim \frac{p}{E} \tag{3}$$

Thus, the deformation of the channel ceiling is proportional to the channel width and not to the channel height. The same argument applies to the sides of the channels, where the lateral strain decay length is now proportional to the channel height h. The scale for the lateral deformation ΔW yields, by analogy,

$$\varepsilon_{lateral} \sim \frac{\Delta W}{h} \sim \frac{p}{E} \tag{4}$$

Comparing eqns (3) and (4) reveals that the lateral deformation ΔW can be neglected in the case where $W \gg h$, and only the top wall will exhibit significant displacement. The relative maximum thickness variation inside the channel at any position z can then be inferred to be:

$$\frac{\Delta h_{max}}{h_0} = c_1 \frac{pW}{Eh_0} \tag{5}$$

where Δh_{max} is the height increase at mid width of the channel under deformation and c_1 is a proportionality constant of magnitude order one. The linearity of this scale was verified numerically using the coupled model described below. Eqn (5) thus provides a natural dimensionless number to characterize the extent of channel deformation. In a channel, when $\Delta p W / Eh_0 \gg 1$, deformation can be neglected. When the channel's aspect ratio is close to 1 ($W \sim h$), the scaling law still holds, but the deformation will occur on the three PDMS walls, assuming that the substrate is glass. However, the Young's

modulus for PDMS is on the order of $E = 1$ MPa (10 atm) so the entire channel is unlikely to deform for $W \sim h$, especially when considering that it is often difficult to impose a pressure much greater than 2 atm before the external fluidic connections begin to leak. The use of eqn (5) for qualitative predictions is still relevant.

Assuming that the channel deflects by a distance Δh_{max} while retaining a rectangular cross-section overestimates the area change and correspondingly, underestimates the true channel resistance. A more accurate scale of the effective channel deflection Δh is to use the width-averaged displacement $<\Delta h>$:

$$\frac{\Delta A}{A_0} = \frac{W \langle \Delta h \rangle}{Wh_0} = \frac{\langle \Delta h \rangle}{h_0} \tag{6}$$

Consequently, at any distance z down the channel, the effective channel height is described by

$$h(z) = h_0 \left(1 + \frac{\langle \Delta h \rangle(z)}{h_0} \right) \tag{7}$$

If the deflection is small, the shape of the deforming wall can be assumed to be parabolic, and the relationship linking the maximum and the average displacement gives $<\Delta h> \sim \frac{2}{3} \Delta h_{max}$. In a first approximation, using eqns (5) and (7), the total height of the channel as a function of position will vary with the local pressure as

$$h(z) = h_0 \cdot \left(1 + \alpha \frac{p(z)W}{Eh_0} \right) \tag{8}$$

where $\alpha = \frac{2}{3} c_1$. From then on, the problem becomes analogous to a flow between tapering plates,[28] where the tapering is a function of the local pressure $p(z)$. To couple the structural deformation to the flow profile, eqn (8) is inserted into the pressure drop flow expression, eqn (2) to yield:

$$-\frac{\partial p(z)}{\partial z} = \frac{12\mu}{h_0^3 W} \left(1 + \alpha \frac{p(z)W}{Eh_0} \right)^{-3} \cdot Q \tag{9}$$

The exact value of α can only be obtained from fluid–materials structure computations. These simulations reveal that the value of α remains approximately constant for a given channel geometry and is on the order of 1. The solution to eqn (9) is equivalent to computing the first order perturbation of the coupled system, assuming the perturbation factor $\alpha p(z)W/Eh_0$ is sufficiently small. The expression is valid provided that the channel remains roughly rectangular in shape, which is not the case for large deformations. Furthermore, at large deformations, $\alpha/c_1 > \frac{2}{3}$ and the ratio must be again computed from numerical simulations. Integrating eqn (9) over the length (L) with the outlet condition $p(z = L) \equiv 0$ gives

$$Q = \frac{h_0^4 E}{48\alpha\mu(L-z)} \left[\left(1 + \alpha \frac{p(z)W}{Eh_0} \right)^4 - 1 \right] \tag{10}$$

The total pressure drop is given by eqn (10) when $z = 0$ and $p(0) = p_0$. When the channel is allowed to deform, eqn (10) predicts that the flow rate will vary non-linearly with the

applied pressure. This behavior can be explained in terms of the combined effect of the 3rd power dependence of the flow rate on the channel height and the linear dependence of the channel vertical displacement on the width. When the perturbation is small, we recover the linear relationship between $p(z)$ and Q (eqn 3). However, when the perturbation becomes large, the flow rate scales as the fourth power of the pressure. When using this result, one must be careful not to overlook the existing pressure drops up and downstream of the channel studied. A non-negligible pressure drop in the outlet tubing, for example, would mean that the effective length L to be used is in fact larger than the channel length. Eqn (10) can be useful in multiple ways: to compute the effective flow rate coming out of a deforming channel, to determine the non-linear pressure distribution in the channel as a function of position z, or to calculate the pressure drop of a channel deforming under an imposed flow rate Q. The major approximation resides in the channel being considered rectangular at all times. Nevertheless, it will be shown that, with α derived from numerical simulations, the perturbation approach is sufficiently robust that the trend holds for deformations of more than 100% of the channel height (see below).

Finally, it is also possible to extract the average cross-sectional velocity distribution $U(z)$ along the channel axis. The conservation of mass inside the channel states that at any axial position z,

$$Q = Wh(z)U(z). \tag{11}$$

Combining eqns (8), (10) and (11) yields

$$U(z) = \frac{Q}{Wh_0}\left(\frac{48\alpha\mu(L-z)Q}{h_0^4 E}+1\right)^{-1/4} \tag{12}$$

The average velocity is no longer a linear function of the flow rate and the fluid acceleration scales as

$$\frac{\partial U}{\partial z} \sim \left[1+\frac{(L-z)}{L_a}\right]^{-5/4} \tag{13}$$

where $L_a = h_0^4 E/48\alpha\mu Q$ is the characteristic acceleration length scale. From eqn (11), we also observe that the height increase and the velocity decrease will compensate each other such that the Reynolds number, $Re = \rho U(z)h(z)/\mu = \rho Q/\mu W$, remains constant independently of the flow rate if we neglect the rounding of the channel cross-section caused by the deformation.

Numerical simulations

Simulations of the interactions between fluid flow and the deformation of PDMS channels were performed using the finite volume method for fluid flow and the finite element method for the channel deformation as implemented in the software CFDACE™ (CFDRC Inc.). The solution strategy was based on reducing the steady state coupled flow-deformation problem into a series of uncoupled problems solved by iterations using a deformable grid. The initial pressure in the channel is used to calculate a displacement solution in the solid. The meshing grid is subsequently

modified using the displacement output. The flow solution is then recalculated with its updated cross-section, yielding a new pressure distribution and velocity field. The new pressure is used to update the grid, and so on, until convergence is achieved. Solutions would typically converge after approximately ten grid update iterations, performed automatically in CFDACE™. Mesh refinement analysis assured that the model error was within 1% of the asymptotic value achievable with a perfectly dense mesh.

To model a semi-infinite medium, a thickness of 2 mm of PDMS was used on top of the channels. This thickness ensured that, for the maximal deflections studied ($\sim$50 μm or 1/40th of the PDMS thickness), the sum of the residual strains at the top of the PDMS were under 3% of the maximum strain observed in the system. In absolute values, the maximum local strains recorded in the PDMS for a 50 μm displacement were 8% while the strain at the boundary was under 0.25%. In theory, the strains should vanish far from the pressure source in an infinitely thick medium. In practice, there is a large computational cost associated with modeling very thick channel walls. Approximating infinity with a 2 mm thick PDMS block was in this case sufficient for an accurate analysis of the problem.

Experimental

Microfluidic setup

Simple linear microfluidic channels were fabricated in poly-(dimethylsiloxane) (Sylgard184™, Corning) using standard soft lithographic procedures.[1] The process yielded channel dimensions of 28 ± 2 μm thick by 1 cm long. Two different widths were studied, 250 μm and 500 μm. Inlets were made wider to ensure a minimal pressure drop in that area (calculated to be around 7% of the pressure drop in the channel). PDMS channels were sealed on a glass cover slip (VWR inc., 170 μm thick) for increased sensitivity in the confocal microscope. Leakage at the inlets was prevented using silicone sealant (Loctite Corp.) and epoxy (Devcon Inc.). Devices were tested to hold pressures higher than 2 bars before leaking.

Special care was taken in preparing the PDMS to use as the bulk of the channel. Temperature, mixing ratios and curing times were carefully controlled to yield PDMS of various elasticity. Their thicknesses were controlled to be larger than 6 mm to ensure that the semi-infinite medium approximation was valid at all observed deformations. PDMS samples from the same batch were tested in compression using a 50 N load cell (Instron Corp.) to determine their Young's moduli. Values between 1 MPa and 3 MPa (±10%) were obtained. Flow through the deforming devices was driven using a conventional syringe pump (Harvard Apparatus Inc.). A piezoelectric pressure sensor (Honeywell Inc.) was used directly upstream of the microchannel to relate the input flow rate to the pressure drop in the device (Fig. 2).

Confocal microscopy

A confocal microscope (Zeiss LSM 510) was used to provide 3D imaging of the deforming channels for various input flow rates. Fluorescein-conjugated Bovine Serum Albumin (FITC-BSA, 0.5 mg ml^{-1}) was used to provide contrast. Confocal
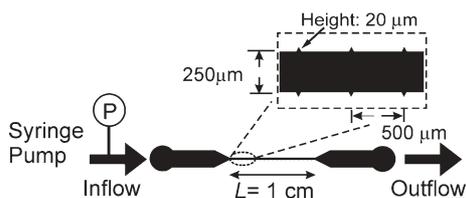
Fig. 2 Schematics of the microfluidic channel used (channel to scale). Deflection is measured in the channel's narrower region (250 μm or 500 μm). A series of triangular ticks (20 μm wide) are patterned at the channel wall every 500 μm for accurate positioning of confocal images.

images were acquired, filtered and rendered using Imaris 4.2 image analysis software (Bitplane Inc.). Cross-section contours were obtained using built-in algorithms from the Matlab image processing toolbox (Mathworks Inc., Natick, MA).

Results and discussion

Numerical simulations

In order to understand the nature of coupled fluid–structure interactions, simulations focus on predicting the extent of the channel deformation as well as the resulting pressure distribution inside the device. The models also reveal the extent of the flow perturbation due to the channel deformation (Fig. 3). These results (and eqn (12) describing the average fluid velocity $U(z)$ at a position z down the channel) show that the average fluid velocity increases towards the channel outlet as the channel cross-section decreases, while the volumetric flow rate remains constant. This acceleration of the flow in a deforming channel is a potential source of error in predicting quantities such as the shear stress in a PDMS device for cell attachment assays.

Confocal imaging and displacement measurements

Channel deformation was verified directly using confocal microscopy. 3D rendered images of the channels capture the
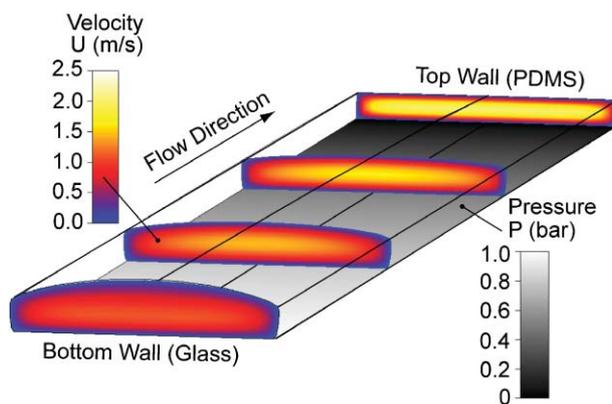
Fig. 3 3D simulation of the velocity (color) and pressure (grayscale) profiles under an imposed pressure drop of 1 bar. The channel geometry represented is 25 μm × 500 μm × 1 cm (Re = 15). Young's modulus is assumed to be of E = 1 MPa. The decreasing cross-sectional area along the channel axis is responsible for the change in the fully developed flow profile and for the acceleration of the flow.
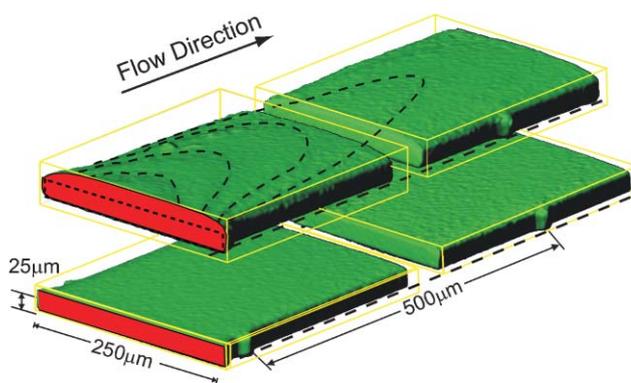
Fig. 4 3D rendering of the entrance of two microfluidic channels of the same material and geometry (250 μm wide, 26 μm thick, 1 cm long, E = 2.2 MPa). Top channel: 300 μL min^{-1} imposed flow rate (Re = 13). The tapering of the channel can be observed by comparing the cross-sections in the first and second segments. Long dash lines: topographic displacement curves. Bottom channel: 1 μL min^{-1} imposed flow rate (no displacement reference measurement).

shape of the channels under various flow conditions (Fig. 4). The experimental data reveal the much higher deformation predicted by the geometry change at the inlets of the device (Fig. 5 and 6, first 3 data points). The rapid tapering of the channel (Fig. 2) effectively produces an unconstrained displacement (stress-free) boundary condition at the edges. Both simulation and experimental data show that this effect dies away within a few widths inside the channel. This entrance effect is not taken into account in the simplified model provided in eqn (10). However, since in most applications, channels are much longer than wide, neglecting it is usually a reasonable approximation.

By using the raw data, measurements of the maximum displacement (located at mid channel width) were performed and compared to the numerical simulations and scaling model (eqn (10)). Two types of measurements were performed in both 250 μm and 500 μm wide channels: (i) A flow rate was specified and the maximum displacement measured for various points along the channel axis (Fig. 5 and 6). (ii) An axial position was
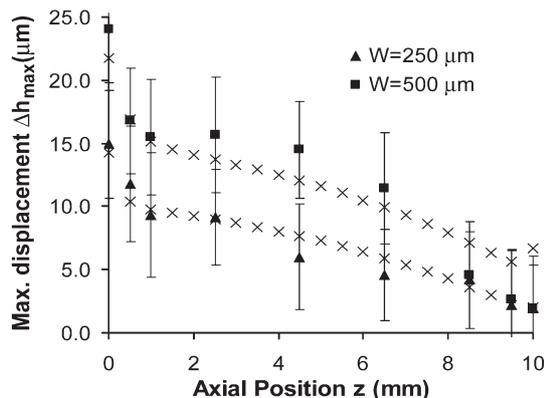
Fig. 5 Maximum displacement *vs.* axial position (E = 2.2 MPa). ▲: 26 μm × 250 μm channel at a flow rate of 300 μL min^{-1}. ■: 30 μm × 500 μm channel at a flow rate of 800 μL min^{-1}. ×: Numerical simulation under the same material and flow conditions.

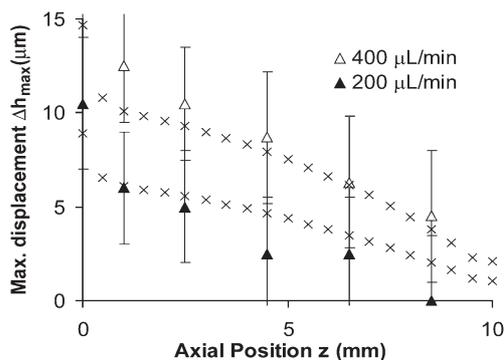**Fig. 6** Maximum displacement as a function of position (26 μm × 250 μm channel, $E = 2.8$ MPa) for $Q = 200$ μL min^{-1} and 400 μL min^{-1}. ×: Numerical simulation under the same material and flow conditions.

specified (specifically, $z = 1$ mm), and the maximum displacement was measured for various imposed flow rates (Fig. 7).

Shapes of the deforming channel cross-sections can be outlined using boundary detection algorithms (Mathworks Inc., Natick, MA) on the confocal data forming the basis for Fig. 4 and Fig. 7. The cross-section shape clearly shows that the side wall deformation, although present, is negligible compared to the extent of the top wall deformation (Fig. 8).

Deformation under pressure-driven flow

The simplest way to demonstrate the severe effects of channel deformation in conventional microfluidic assays is to monitor the relationship between the total pressure drop over a channel section and the resulting flow rate (and *vice versa*). In a perfectly rigid channel, the pressure drop will vary linearly with the imposed flow rate, as described in eqn (2). Fig. 9 shows the flow rate as a function of the measured pressure for two channel geometries and two different elastic moduli E. The flow rates are much higher than the ones predicted in non-deforming channels. For example, in a 30 μm × 500 μm cross-section channel ($E = 2.2$ MPa), the expected flow rate in a rigid channel under a pressure of 1 bar is 270 μL min^{-1} while it is measured to be 1600 μL min^{-1} in the deforming channel – a
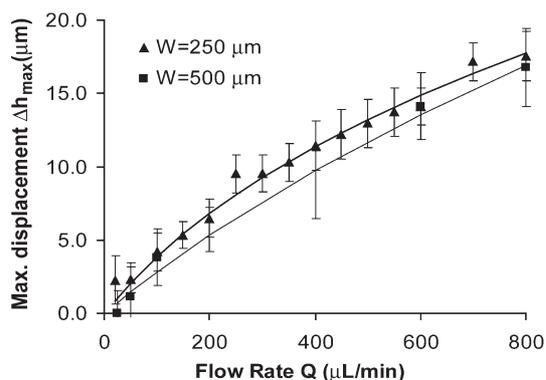

Fig. 7 Maximum deformation *vs.* flow rate ($E = 2.2$ MPa). —: fit from eqn (10) using the displacement expression $h = h_0 + c_1 p W/E$. The fit parameter yields $c_1 = 0.73$ (250 μm channel) and $c_1 = 0.42$ (500 μm channel).

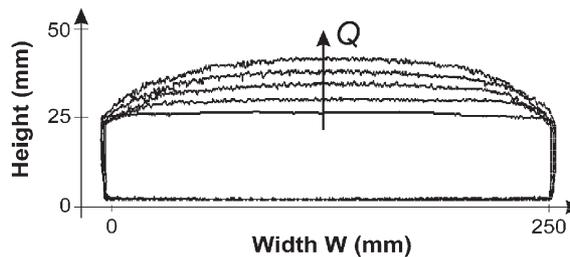**Fig. 8** Measured cross-section profile at axial position $z = 1$ mm for imposed flow rates $Q = 1, 100, 300, 500, 700$ μL min^{-1}. 26×250 μm^2 initial cross-section, $E = 2.2$ MPa.
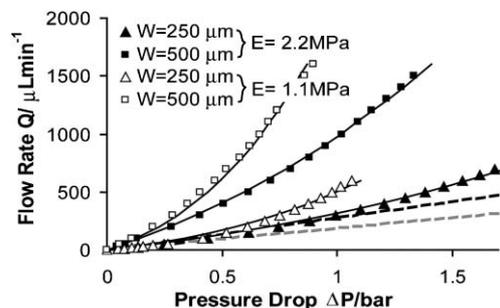

Fig. 9 Channel flow rate as a function of channel pressure drop. Dashed lines: expected flow rate in the absence of channel deformation (eqn 2) for $W = 250$ μm and $W = 500$ μm. Solid lines: fit of eqn (10) to the data. $\alpha = 0.33$ (30 μm × 500 μm, −2.2 MPa), $\alpha = 0.55$ (26 μm × 250 μm, −2.2 MPa), $\alpha = 0.67$ (26 μm × 250 μm, −1.1 MPa), and $\alpha = 0.56$ (26 μm × 500 μm, −1.1 MPa). Re numbers varied from 0 to 100 in this experiment.

∼500% increase in flow rate. Forming the ratio of flow rates predicted by eqns (2) and (10) yields the following scaling relationship for the amount of increased flow rate at small deformations ($\Delta h/h_0 \gg 1$):

$$\frac{\Delta Q}{Q} = \frac{Q_{\text{deform}} - Q_{\text{rigid}}}{Q_{\text{rigid}}} \sim \frac{3\alpha}{2} \frac{\Delta p W}{E h_0} \qquad (14)$$

Thus, if the channel were 100 μm thick, other factors remaining the same, the relative variation in the flow rate would be only ∼25%. However, a 5 μm thick channel would suffer from a 25-fold deviation in the expected flow rate. The height dependence is expected to be even more important at larger deformations ($\Delta Q/Q \sim (\Delta h/h_0)^4$). Consequently, deformations impose a severe constraint on the design and operation of PDMS channel networks at the scale of a few microns.

Conclusion

Rapid prototyping in PDMS possesses many advantages, *e.g.*, low cost and quick turnaround time. However, at the micron scale, channel deformation effect becomes important and must be quantified for predictable assay performance. The dimensionless number ($\Delta p W/E h_0$) provides a simple means to assess whether deformation needs to be considered. The experimental results and numerical simulations point to 3 main consequences of channel deformation.

(1) Cross-section effects

For a channel with high aspect ratio (width to height), the amount of deflection under pressure is proportional to the channel width and not influenced by the channel height h or the PDMS wall thickness H provided that $(\Delta h_{max} \gg H)$. Shallower channels will suffer relatively larger changes in their cross-sectional areas and thus be more sensitive to deformation. Herein, we used a typical channel height of $\sim 25\ \mu m$ since their deformation is easily detectable by confocal imaging. However, the effect would have been markedly larger in, say, 5 μm high channels.

(2) Stream-wise effects

Channel deformation decreases non-linearly along the length of the channel to near zero at the outlet (depending on the outlet pressure conditions). This decrease in cross-sectional area causes a corresponding acceleration of the fluid velocity along the axis with related variations in diffusion/convection time scales and shear stresses. These effects complicate the development of any assay relying on fluid transport to the surface or shear stress measurements.

(3) Flow rates and pressure effects

For a given flow rate, the pressure drop in a deformable channel will be much less than that of a rigid channel. Thus, deformable devices will typically be able to handle much higher flow rates than expected without leaking due to the channel compliance.

Increasing the rigidity of polymer channels will decrease the amount of deformation and thus reduce the effects. Possible ways to achieve higher effective bulk moduli vary. Curing PDMS for longer times (>24 h) at higher temperatures ($120\ ^{\circ}C$) with more curing agent have been reported to increase the elasticity modulus of PDMS to $E = 4$ MPa.[29] Encasing glass microslides close to the channel surface in the unbaked polymer is another example of a simple way to avoid large deformations and their corresponding effects in PDMS-based microfluidic systems.

Appendix: Elasticity problem formulation

We refer the reader to the book by Sadd[26] for a more complete development of the elasticity equations. In absence of body forces, the internal displacement equations governing elastic deformation are described by Lamé's equation:

$$\vec{\nabla}^2 \vec{u} + \left(\frac{2v}{(1-2v)} \right) \vec{\nabla} \left(\vec{\nabla} \cdot \vec{u} \right) = \vec{0} \qquad (A1)$$

where the displacement vector is given by

$$\vec{u} = u_1(x, y, z)\hat{x}_1 + u_2(x, y, z)\hat{x}_2 + u_3(x, y, z)\hat{x}_3 \qquad (A2)$$

The unit vectors $\hat{x}_i$ point in the direction of x, y and z. At the interface of the PDMS block, the boundary conditions are of a third kind (mixed traction and displacement) and read:

$$\vec{u} = \vec{0}, \text{ for glass} - \text{PDMS interface} \qquad (A3a)$$

$$\underline{\sigma} \cdot \vec{n} = p(z)\vec{n}, \text{ for fluid} - \text{PDMS interface} \qquad (A3b)$$

where $\vec{n}$ is the unit vector normal to the interface. Using the displacement formulation and Hooke's generalized law, the stress value can be converted to strain values and thus to displacement. Lumping these steps together provide the stress–displacement relationships in the PDMS.

$$\sigma_{ij} = \frac{Ev}{(1-2v)(1+v)} \vec{\nabla} \cdot \vec{u} \delta_{ij} + \frac{E}{(1+v)} \left(\frac{\partial u_i}{\partial x_j} + \frac{\partial u_j}{\partial x_i} \right) \qquad (A4)$$

The elasticity equations are coupled to Navier–Stokes flow by the pressure $p(z)$ in eqn (1). When dealing with numerical simulations in incompressible media, a Poisson ratio of $v = 0.499$ is used in CFDACE instead of $v = 0.5$ to prevent the numerical divergence of the problem.

References

1 Y. Xia and G. M. Whitesides, *Annu. Rev. Mater. Sci.*, 1998, **28**, 153.
2 G. M. Whitesides and D. E. Ingber, *Annu. Rev. Biomed. Eng.*, 2001, **3**, 335.
3 S. R. Quake and A. Scherer, *Science*, 2000, **290**, 1536.
4 R. Kane, D. E. Ingber and G. M. Whitesides, *Biomaterials*, 1999, **20**, 2363.
5 J. C. Lotters, W. Olthuis, P. H. Veltink and P. Bergveld, *J. Micromech. Microeng.*, 1997, **7**, 145.
6 S. D. Senturia, *Microsystem Design*, Kluwer Academic, Dordrecht, The Netherlands, 2001.
7 T. Thorsen, S. J. Maerkl and S. R. Quake, *Science*, 2002, **298**, 580.
8 M. A. Unger, H. P. Chou, T. Thorsen, A. Scherer and S. R. Quake, *Science*, 2000, **288**, 113.
9 A. Y. Fu, H. P. Chou, C. Spence, F. H. Arnold and S. R. Quake, *Anal. Chem.*, 2002, **74**, 2451.
10 J. W. Hong, V. Studer, G. Hang, W. F. Anderson and S. R. Quake, *Nat. Biotehnol.*, 2004, **22**, 435.
11 K. Hosokawa, K. Hanada and R. Maeda, *J. Micromech. Microeng.*, 2002, **12**, 1.
12 E. Delamarche, H. Schmid, B. Michel and H. Biebuyck, *Adv. Mater.*, 1997, **9**, 741.
13 C. Y. Hui, A. Jagota, Y. Y. Lin and E. J. Kramer, *Langmuir*, 2002, **18**, 1394.
14 J. Happel and H. Brenner, *Low Reynolds Number Hydrodynamics*, Prentice Hall, New York, 1965.
15 S. K. Murthy, A. Sin, R. G. Tompkins and M. Toner, *Langmuir*, 2004, **20**, 11649.
16 H. Lu, L. Y. Koo, W. M. Wang, D. A. Lauffenburger, L. G. Griffith and K. F. Jensen, *Anal. Chem.*, 2004, **76**, 5257.
17 A. S. Kantak, B. K. Gale, Y. Lvov and S. A. Jones, *Biomed. Microdevices*, 2003, **5**, 207.
18 T. Gervais and K. F. Jensen, *Chem. Eng. Sci.*, 2006, **61**, 1102.
19 C. Wofsy and B. Goldstein, *Biophys. J.*, 2002, **82**, 1743.
20 M. Furuki, J. Kameoka, H. G. Craighead and M. S. Isaacson, *Sens. Actuators, B*, 2001, **79**, 63.
21 H. Song and R. F. Ismagilov, *J. Am. Chem. Soc.*, 2003, **125**, 14613.
22 A. Manz, N. Graber and H. M. Widmer, *Sens. Actuators, B*, 1990, **1**, 244.
23 M. A. Holden, S. Kumar, A. Beskok and P. S. Cremer, *J. Micromech. Microeng.*, 2003, **13**, 412.
24 H. G. Poulos and E. H. Davis, *Elastic solutions for soil and rock mechanics*, ed. T. W. Lambe, John Wiley & Sons, New York, NY, 1974.
25 S. P. Timoshenko and J. N. Goodier, *Theory of elasticity*, McGraw-Hill, New York, NY, 1970.

26 M. H. Sadd, *Elasticity theory, applications, and numerics*, Elsevier Butterworth Heinemann, New York, NY, 2005.

27 T. Gervais, Mass Transfer and Structural Analysis of Microfluidic Sensors, *Ph.D. thesis*, Massachusetts Institute of Technology, Cambridge, MA, 2005.

28 W. M. Deen, *Analysis of Transport Phenomena*, Oxford University Press, New York, NY, 1998.

29 B. Michel, in 'Limited stability of molded features in elastomeric materials: Stamp material Sylgard 184®', http://www.zurich.ibm.com/st/microcontact/stamps/material.html, 2005.